SCIENCE CHINA
Information Sciences

• RESEARCH PAPER •

September 2020, Vol. 63 192301:1–192301:12
https://doi.org/10.1007/s11432-019-2799-y

Hybrid beamforming design for mmWave OFDM distributed antenna systems

Yu ZHANG[1], Dongming WANG[1,2*], Yiming HUO[3], Xiaodai DONG[3] & Xiaohu YOU[1,2]

[1]*National Mobile Communications Research Laboratory, Southeast University, Nanjing* 210096*, China;*
[2]*Purple Mountain Laboratory, Southeast University, Nanjing* 211111*, China;*
[3]*Department of Electrical and Computer Engineering, University of Victoria, Victoria,* V8P 5C2*, Canada*

Received 12 August 2019/Revised 24 October 2019/Accepted 16 February 2020/Published online 28 July 2020

Abstract This paper presents a hybrid beamforming design for millimeter-wave (mmWave) orthogonal frequency division multiplexing (OFDM) distributed antenna systems (DASs). First, we derive a downlink signal transmission model that considers the delay spread differences (DSDs) caused by the distributed nature of the network. We then propose a cooperative wideband hybrid beamforming method under the transmitting power constraints of each remote access unit. In a simulation study, the proposed method performed comparably to fully-digital beamforming, even when operated with practical finite-resolution phase shifters. We further confirm that the DSDs are the dominant cause of performance degradation in mmWave OFDM DASs.

Keywords hybrid beamforming, distributed antenna systems, millimeter wave, OFDM, delay spread differences, synchronization

Citation Zhang Y, Wang D M, Huo Y M, et al. Hybrid beamforming design for mmWave OFDM distributed antenna systems. Sci China Inf Sci, 2020, 63(9): 192301, https://doi.org/10.1007/s11432-019-2799-y

1 Introduction

Distributed antenna systems (DASs), composed of geographically separated remote access units (RAUs), provide sufficient spatial degrees of freedom (DoFs) to facilitate ultra-high speed wireless communications [1–3]. Such a distributed architecture is very suitable for radio transmission in millimeter-wave (mmWave) frequency bands [4–7]. First, the densely deployed low-power RAUs can shorten the distances between transceivers, thus compensating for the significant propagation loss at high frequencies; second, they are highly resistant to the severe blockage effect in mmWave channels. Therefore, DAS technology combined with mmWave transmission is envisioned to play a crucial and promising role in fifth generation (5G) and beyond communications.

Most of the aforementioned studies on mmWave DASs, e.g., Refs. [5–7] are restricted to the flat-fading channel model. However, in practical applications of mmWave DASs, the sparse multipath and tremendously wide signal bandwidth lead to frequency-selective channels [8]. Orthogonal frequency division multiplexing (OFDM) modulation can divide the frequency-selective channel into a continuous set of frequency-flat subcarriers with scalar gains [9]. Consequently, mmWave OFDM DASs are promising network architectures enabling practical and commercial application scenarios, such as mobile broadband communications for high-speed trains [10], distributed and multi-layer unmanned aerial vehicles network architectures for Internet-of-Things and beyond 5G applications [11].

* Corresponding author (email: wangdm@seu.edu.cn)

Unlike the traditional fully-digital structure with one dedicated radio frequency (RF) chain for each antenna element, the hybrid analog-digital architecture strikes a balance between performance gain and hardware complexity [12, 13]. Therefore, it is ideally suited to mmWave DASs. As corroborated in [7], the distributed sub-array architecture of the hybrid analog-digital processing configuration enables significantly higher diversity gain than the collocated antenna architecture. Furthermore, the authors of [6] proposed a distributed multi-RF chain hybrid mmWave scheme for a densely distributed small-cell-base-stations system which exploits the DoFs to improve the data multiplexing. In our experience, most of the emerging literature related to hybrid precoding in mmWave OFDM systems covers only multiple-in multiple-out (MIMO) or single-cell multi-user scenarios. For example, the authors of [14] proposed an efficient hybrid precoding algorithm that leverages the penalty decomposition method for wideband MIMO systems. Assuming cooperative users, Sohrabi and Yu [13] developed a hybrid precoding design for a mmWave single-cell multi-user system deployed with a large-scale antenna array. A hybrid precoding approach enabled by an alternating direction method of multipliers has been recently developed based on an alternating optimization framework in a distributed phased arrays based MIMO system [15–17]. However, no published work has investigated hybrid beamforming design in mmWave OFDM DASs. The main challenge of mmWave OFDM DASs hybrid beamforming design is collaborating wideband hybrid beamformers under per-RAU power constraints. Specifically, each RAU requires a common analog beamformer shared across all subcarriers and an individual digital beamformer on different subcarriers.

Wideband wireless data transmission is mainly limited by the multipath delay spread (DS), which induces a frequency-selective effect. For instance, at an mmWave BS employing OFDM modulation, the transmitted signal becomes sensitive to the propagation delay of channels across the large array aperture. With antenna level synchronization, the cyclic prefix (CP) length must be increased to cope with the increased DS [18]. Additionally, You et al. [19] proposed a new concept of beam level synchronization that decreases the effective delay and Doppler frequency spread in mmWave massive MIMO systems. Nevertheless, multiple transmitted signals from multiple distributed RAUs in DASs arrive at the same user equipment (UE) at different times, which is more complicated and stringent than the collocated antenna configuration such as [18, 19], and results in DS differences (DSDs). After a UE completes the timing acquisition of the received RAU signals, the DSDs generate a timing offset. A pioneering work [20] has investigated the asynchronous reception effects caused by DSDs on distributed massive MIMO-OFDM systems at microwave frequencies. The same effect has been observed in a distributed MIMO prototyping system [21]. However, to our knowledge, the impact of DSDs on mmWave DASs with hybrid structures has not been investigated.

In this paper, we first derive the equivalent channel model revealing the effect of DSDs on mmWave OFDM DASs. We then design a cooperative hybrid beamforming algorithm for mmWave DASs under per-RAU transmitting power constraints within the penalty dual decomposition (PDD) framework [22,23]. To verify the effectiveness of the proposed hybrid beamforming algorithm, we also develop a quasi-Newton based fully-digital beamforming algorithm as a baseline (see Appendix B for a detailed derivation). Finally, we demonstrate the superior performance of the proposed hybrid beamforming algorithm in simulations, and numerically investigate the impact of DSDs on mmWave DASs.

Notations. Upper and lower case boldface letters denote matrices and column vectors, respectively. blkdiag$\{\cdot\}$ denotes a block diagonal matrix whose diagonal entries are matrices. Tr$\{\cdot\}$ denotes the matrix trace operation. $(\cdot)^{\mathrm{H}}$, $(\cdot)^{\mathrm{T}}$, $(\cdot)^*$ and $(\cdot)^\dagger$ stand for the conjugate transpose, transpose, conjugate, and pseudo-inverse, respectively. $|\cdot|$ and $\Re\{\cdot\}$ denotes the absolute value and real part of a complex scalar. $\|\cdot\|$ denotes the Frobenius norm of a complex matrix. $[\cdot]_{i,j}$, $[\cdot]_{i,:}$ and $[\cdot]_{:,j}$ represent the (i,j)th element, ith row and jth column of any matrix, respectively. $\mathcal{CN}(\boldsymbol{\mu}, \boldsymbol{R})$ denotes the complex Gaussian distribution with mean $\boldsymbol{\mu}$ and covariance matrix $\boldsymbol{R}$. $\jmath = \sqrt{-1}$ and $\delta(\cdot)$ denotes the imaginary unit and the Dirac delta function, respectively. The notation $\triangleq$ is used for definitions. $\mathcal{U}(a, b)$ denotes a uniform distribution taking values between a and b.

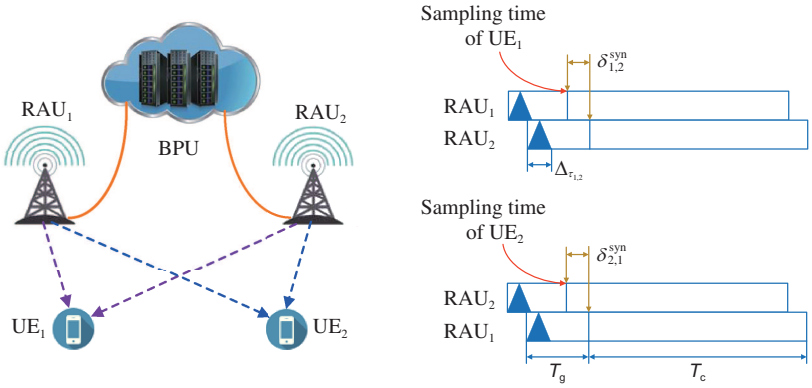

Figure 1 (Color online) An illustration of the effect of DSDs on downlink (DL) transmission in mmWave OFDM DASs, e.g., in the case of two RAUs and two UEs.

2 System model

Consider a mmWave DAS consisting of M randomly distributed RAUs serving K single-antenna UE within the coverage area. Each RAU has $N_{\rm A}$ antennas and $N_{\rm RF}$ RF chains and is connected to a central baseband processing unit (BPU) via high-speed fronthaul links as shown in Figure 1. Define $N_{\rm A}^{\rm tot} \triangleq MN_{\rm A}$ and $N_{\rm RF}^{\rm tot} \triangleq MN_{\rm RF}$. The impulse response for the DL channel between RAU m and UE k is represented as follows [24]:

$$\breve{\boldsymbol{h}}_{k,m}^{\rm H}[\tau] = \sqrt{\frac{N_{\rm A}}{L}}\beta_{k,m}\sum_{\ell=1}^{L}\alpha_{k,m,\ell}\boldsymbol{v}_{\rm rau}^{\rm H}\left(\theta_{k,m,\ell}\right)\delta\left(\tau-\tau_{k,m,\ell}\right), \tag{1}$$

where $\beta_{k,m}$ accounts for the corresponding average large-scale path loss, $\alpha_{k,m,\ell} \sim \mathcal{CN}(0,1)$ represents the normalized complex gain for path ℓ, $\tau_{k,m,l}$ is the path delay, $\theta_{k,m,l} \in [0, 2\pi)$ is the angle of departure (AoD) and the array response vector is given by

$$\boldsymbol{v}_{\rm rau}(\theta) = \frac{1}{\sqrt{N_{\rm A}}}\left[1, {\rm e}^{\jmath\pi\sin\theta}, \ldots, {\rm e}^{\jmath\pi(N_{\rm A}-1)\sin\theta}\right]^{\rm T}. \tag{2}$$

Consider a wideband DAS employing OFDM modulation with the number of subcarriers, $N_{\rm c}$, and the cyclic prefix (CP), $N_{\rm g}$ samples. Then the OFDM symbol length and the CP length are $T_{\rm c} = N_{\rm c}T_{\rm s}$ and $T_{\rm g} = N_{\rm g}T_{\rm s}$, respectively, where $T_{\rm s}$ is the system sampling interval. For the transmission, the BPU first precodes K data symbols $s_k[n]$ at each subcarrier by using a low-dimensional digital precoder:

$$\boldsymbol{f}_{{\rm B},k}[n] = \left[\boldsymbol{f}_{{\rm B},k,m}^{\rm T}[n], \ldots, \boldsymbol{f}_{{\rm B},k,M}^{\rm T}[n]\right]^{\rm T} \in \mathbb{C}^{N_{\rm RF}^{\rm tot}\times 1}, \tag{3}$$

where $\boldsymbol{f}_{{\rm B},k,m}[n] \in \mathbb{C}^{N_{\rm RF}\times 1}$ is the digital precoder of UE k at RAU m, then transforms the signals to the time domain by using $N_{\rm RF}^{\rm tot}$ parallel K-point inverse fast Fourier transform (IFFT). Next, the BPU distributes the signals to all the RAUs via the fronthaul links. After adding CPs, each RAU employs an analog beamforming matrix, $\boldsymbol{F}_{{\rm R},m} \in \mathbb{C}^{N_{\rm A}\times N_{\rm RF}}$, which is identical for all subcarriers [13]. In fact, this analog beamforming matrix is composed of phase shifters (PSs) with constant modulus constraints, i.e., $|[\boldsymbol{F}_{{\rm R},m}]_{i,j}| = 1$, for $\forall i, j$. Consequently, the final transmitted signal at subcarrier n of RAU m is written as follows:

$$\boldsymbol{x}_m[n] = \boldsymbol{F}_{{\rm R},m}\sum_{k=1}^{K}\boldsymbol{f}_{{\rm B},k,m}[n]s_k[n]. \tag{4}$$

Considering one given OFDM transmission block, the discrete-time transmitted signal at RAU m is represented as

$$\breve{\boldsymbol{x}}_m\left[qT_{\rm s}\right] = \frac{1}{N_{\rm c}}\sum_{n=0}^{N_{\rm c}-1}\boldsymbol{x}_m[n]{\rm e}^{\jmath 2\pi\frac{n}{N_{\rm c}}q}, \tag{5}$$

where $-N_{\mathrm{g}} \leqslant q \leqslant N_{\mathrm{c}}-1$. Thus, the received signal at UE k from RAU m is given by

$$\breve{y}_{k,m}\left[qT_{\mathrm{s}}\right]=\int_{\tau_{k,m}^{\min}}^{\tau_{k,m}^{\max}} \breve{\boldsymbol{h}}_{k,m}^{\mathrm{H}}[\tau]\breve{\boldsymbol{x}}_m\left[qT_{\mathrm{s}}-\tau\right]\mathrm{d}\tau+\breve{z}_{k,m}\left[qT_{\mathrm{s}}\right], \tag{6}$$

where $\breve{z}_{k,m}[qT_{\mathrm{s}}]$ is the sampled additive Gaussian noise and the received signal experiences time offsets relative to the transmitted signal ranging from $\tau_{k,m}^{\min} \triangleq \min_{\ell}\ \tau_{k,m,\ell}$ to $\tau_{k,m}^{\max} \triangleq \max_{\ell}\ \tau_{k,m,\ell}$. Then, the DS is defined as

$$\Delta_{\tau_{k,m}} \triangleq \tau_{k,m}^{\max}-\tau_{k,m}^{\min}. \tag{7}$$

We assume the time synchronization is performed at the UE side. Since M RAUs are distributed at different locations, the propagation time from these RAUs to any fixed UE is different. Therefore, with the synchronization point accommodating the first arrived OFDM symbol at UE k [20], the calibration for compensating the time offsets of the received signals is chosen as

$$\tau_k^{\mathrm{syn}} \triangleq \min_{m}\ \tau_{k,m}^{\min}. \tag{8}$$

In addition, the value of DSDs from RAU m to UE k is denoted as

$$\delta_{k,m}^{\mathrm{syn}} \triangleq \tau_{k,m}^{\min}-\tau_k^{\mathrm{syn}}. \tag{9}$$

For clarity, we give an illustration of the effect of DSDs in mmWave OFDM DASs for the case of two RAUs and UEs in Figure 1. We set the time as 0 at UE 1 when the first symbol of RAU 1 arrives. Then, the first symbol of RAU 2 will experience time delay $\delta_{1,2}^{\mathrm{syn}}$ relative to the first symbol of RAU 1, which brings the sampling offset to the transmitted signal of RAU 2. Therefore, a synchronous sampling clock for all the UEs is not required for realization. Since the mmWave RAUs serving any fixed UE are not largely separate, the CP length can be carefully chosen in DASs to satisfy $T_{\mathrm{g}} \geqslant \max_{k,m}\{\Delta_{\tau_{k,m}}+\delta_{k,m}^{\mathrm{syn}}\}$ to prevent the inter-carrier interference (ICI) [18, 19].

Having received the delayed transmitted signals from all the RAUs, each UE applies the CP removal and then FFT operations to the synchronized received signal. Thus, the demodulated signal at UE k from RAU m in the frequency domain can be expressed as

$$y_{k,m}^{\mathrm{syn}}[n]=\sum_{q=0}^{N_{\mathrm{c}}-1}\breve{y}_{k,m}\left[qT_{\mathrm{s}}+\tau_k^{\mathrm{syn}}\right]\mathrm{e}^{-\jmath 2\pi\frac{n}{N_{\mathrm{c}}}q}. \tag{10}$$

By substituting the frequency domain representation of the signal transmission in (6), i.e., $y_{k,m}[n]=\boldsymbol{h}_{k,m}^{\mathrm{H}}[n]\boldsymbol{x}_m[n]+z_{k,m}\left[n\right]$, where the channel response in the frequency domain corresponding to (1) is

$$\boldsymbol{h}_{k,m}^{\mathrm{H}}[n]=\sqrt{\frac{N_{\mathrm{A}}}{L}}\beta_{k,m}\sum_{\ell=1}^{L}\alpha_{k,m,\ell}\boldsymbol{v}_{\mathrm{rau}}^{\mathrm{H}}\left(\theta_{k,m,\ell}\right)\mathrm{e}^{-\jmath 2\pi\frac{n}{N_{\mathrm{c}}}\frac{\tau_{k,m,\ell}}{T_{\mathrm{s}}}}, \tag{11}$$

we can transform (10) into the following form:

$$\begin{aligned} y_{k,m}^{\mathrm{syn}}[n] &= \frac{1}{N_{\mathrm{c}}}\sum_{q=0}^{N_{\mathrm{c}}-1}\left\{\sum_{n'=0}^{N_{\mathrm{c}}-1}y_{k,m}[n']\mathrm{e}^{\jmath 2\pi\frac{n'}{N_{\mathrm{c}}}\frac{\tau_k^{\mathrm{syn}}}{T_{\mathrm{s}}}}\mathrm{e}^{\jmath 2\pi\frac{q}{N_{\mathrm{c}}}n'}\right\}\mathrm{e}^{-\jmath 2\pi\frac{q}{N_{\mathrm{c}}}n} \\ &= \frac{1}{N_{\mathrm{c}}}\sum_{n'=0}^{N_{\mathrm{c}}-1}y_{k,m}[n']\mathrm{e}^{\jmath 2\pi\frac{n'}{N_{\mathrm{c}}}\frac{\tau_k^{\mathrm{syn}}}{T_{\mathrm{s}}}}\cdot\sum_{q=0}^{N_{\mathrm{c}}-1}\mathrm{e}^{\jmath 2\pi\frac{q}{N_{\mathrm{c}}}(n'-n)} \\ &= \boldsymbol{g}_{k,m}^{\mathrm{H}}[n]\boldsymbol{x}_{k,m}[n]+z_{k,m}[n], \end{aligned} \tag{12}$$

where the variable n' also denotes the frequency index to be distinguished from the indicator n, the last equality follows from the geometric progression property, i.e., $\sum_{q=0}^{N_{\mathrm{c}}-1}\mathrm{e}^{\jmath 2\pi\frac{q}{N_{\mathrm{c}}}(n'-n)}=N_{\mathrm{c}}\cdot\delta(n'-n)$, and the equivalent DL channel consisting of two parts is defined as

$$\boldsymbol{g}_{k,m}^{\mathrm{H}}[n] \triangleq \underbrace{\boldsymbol{h}_{k,m}^{\mathrm{H}}[n]\cdot\mathrm{e}^{\jmath 2\pi\frac{n}{N_{\mathrm{c}}}\frac{\tau_{k,m}^{\min}}{T_{\mathrm{s}}}}}_{\triangleq\overline{\boldsymbol{h}}_{k,m}^{\mathrm{H}}[n]}\cdot\underbrace{\mathrm{e}^{-\jmath 2\pi\frac{n}{N_{\mathrm{c}}}\frac{\delta_{k,m}^{\mathrm{syn}}}{T_{\mathrm{s}}}}}_{\text{synchronization error}}, \tag{13}$$

where $\bar{\boldsymbol{h}}_{k,m}^{\mathrm{H}}[n]$ is the single-RAU synchronized DL channel and the last part is the frequency-dependent synchronization error caused by DSDs. In fact, the effect of DSDs is a generalization to the spatial-wideband effect [18] wherein the time difference between any two antennas can be accurately calculated based on the array manifold.

Finally, the demodulated signal at UE k from all the RAUs admits the following:

$$y_k^{\mathrm{syn}}[n] = \boldsymbol{g}_k^{\mathrm{H}}[n]\boldsymbol{F}_{\mathrm{R}}\boldsymbol{f}_{\mathrm{B},k}[n]s_k[n] + \sum_{u\neq k}^{K}\boldsymbol{g}_k^{\mathrm{H}}[n]\boldsymbol{F}_{\mathrm{R}}\boldsymbol{f}_{\mathrm{B},u}[n]s_u[n] + z_k[n], \tag{14}$$

where $z_k[n] \sim \mathcal{CN}(0,\sigma_{\mathrm{z}}^2)$ is the additive Gaussian noise, the equivalent DL channel between UE k and all the RAUs is given by

$$\boldsymbol{g}_k^{\mathrm{H}}[n] = \left[\boldsymbol{g}_{k,1}^{\mathrm{H}}[n],\ldots,\boldsymbol{g}_{k,M}^{\mathrm{H}}[n]\right], \tag{15}$$

and the whole RF precoder is a block diagonal matrix denoted as

$$\boldsymbol{F}_{\mathrm{R}} = \mathrm{blkdiag}\left\{\boldsymbol{F}_{\mathrm{R},1},\ldots,\boldsymbol{F}_{\mathrm{R},M}\right\}. \tag{16}$$

3 Cooperative hybrid beamforming design

3.1 Problem formulation

In this subsection, we assume the BPU only has access to the single-RAU synchronized DL channels of the UEs, i.e., $\{\bar{\boldsymbol{h}}_{k,m}[n]\}$, so that the DSDs effects can be studied without the influence of channel estimation errors [20]. Sequentially, we aim to design hybrid beamformers to maximize the sum rate over all subcarriers. The original problem is formulated as

$$\max_{\boldsymbol{F}_{\mathrm{R}},\{\boldsymbol{f}_{\mathrm{B},k}[n]\}} \quad \sum_{k=1}^{K}\sum_{n=1}^{N_{\mathrm{c}}}\log\left(1+\frac{\left|\bar{\boldsymbol{h}}_k^{\mathrm{H}}[n]\boldsymbol{F}_{\mathrm{R}}\boldsymbol{f}_{\mathrm{B},k}[n]\right|^2}{\sum_{u\neq k}^{K}\left|\bar{\boldsymbol{h}}_k^{\mathrm{H}}[n]\boldsymbol{F}_{\mathrm{R}}\boldsymbol{f}_{\mathrm{B},u}[n]\right|^2+\sigma_{\mathrm{z}}^2}\right) \tag{17a}$$

$$\text{s.t.} \quad \sum_{k=1}^{K}\sum_{n=1}^{N_{\mathrm{c}}}\left\|\boldsymbol{\Xi}_m\boldsymbol{F}_{\mathrm{R}}\boldsymbol{f}_{\mathrm{B},k}[n]\right\|^2 \leqslant P_{\max}^{\mathrm{rau}},\ \forall m, \tag{17b}$$

$$\boldsymbol{F}_{\mathrm{R}} = \mathrm{blkdiag}\left\{\boldsymbol{F}_{\mathrm{R},1},\ldots,\boldsymbol{F}_{\mathrm{R},M}\right\}, \tag{17c}$$

$$\left|[\boldsymbol{F}_{\mathrm{R},m}]_{i,j}\right| = 1,\ \forall i,j,m, \tag{17d}$$

where $\boldsymbol{\Xi}_m = [\boldsymbol{0}_{N_{\mathrm{A}}\times(m-1)N_{\mathrm{A}}}, \boldsymbol{I}_{N_{\mathrm{A}}}, \boldsymbol{0}_{N_{\mathrm{A}}\times(M-m)N_{\mathrm{A}}}]$ is a selection matrix for RAU m. Note that in order to examine the effect of DSDs on mmWave OFDM DASs, the ideal hybrid beamformer is designed based on the equivalent DL channel in (13).

3.2 Beamforming design

To tackle the nonconvex objective function in problem (17), we rewrite it into an equivalent yet more tractable form by introducing the auxiliary variables, i.e., the receiver gain $a_k[n]$ and positive weight coefficient $w_k[n]$, $\forall k,n$. Thus, problem (17) can be equivalently transformed into the following weighted mean-square error (MSE) form [25]

$$\max_{\boldsymbol{F}_{\mathrm{R}},\{a_k[n],w_k[n],\boldsymbol{f}_{\mathrm{B},k}[n]\}} \quad \sum_{k=1}^{K}\sum_{n=1}^{N_{\mathrm{c}}}\left(\log\left(w_k[n]\right) - w_k[n]e_k[n]\right) \tag{18a}$$

$$\text{s.t.} \quad \text{(17b), (17c), and (17d)}, \tag{18b}$$

where the MSE of UE k at subcarrier n is defined as

$$e_k[n] \triangleq \left|1-a_k^*[n]\bar{\boldsymbol{h}}_k^{\mathrm{H}}[n]\boldsymbol{F}_{\mathrm{R}}\boldsymbol{f}_{\mathrm{B},k}[n]\right|^2 + |a_k[n]|^2\left(\sigma_{\mathrm{z}}^2+\sum_{u\neq k}^{K}\left|\bar{\boldsymbol{h}}_k^{\mathrm{H}}[n]\boldsymbol{F}_{\mathrm{R}}\boldsymbol{f}_{\mathrm{B},u}[n]\right|^2\right). \tag{19}$$

The detailed proof of the equivalence between problem (17) and (18) can be found in Appendix A.

However, problem (18) is still difficult to solve due to the unit modulus constraints induced by PSs, and the coupling between the analog and digital beamforming vectors. Hence, by introducing new auxiliary variables $\boldsymbol{x}_k[n]$ and $\boldsymbol{y}_{m,k}[n]$, problem (18) can be equivalently transformed into

$$\max_{\mathcal{Z}} \quad \sum_{k=1}^{K}\sum_{n=1}^{N_{\rm c}} \left(\log\left(w_k[n]\right) - w_k[n]\bar{e}_k[n]\right) \tag{20a}$$

$$\text{s.t.} \quad \sum_{k=1}^{K}\sum_{n=1}^{N_{\rm c}} \left\|\boldsymbol{y}_{m,k}[n]\right\|^2 \leqslant P_{\max}^{\rm rau},\ \forall m, \tag{20b}$$

$$\boldsymbol{x}_k[n] = \boldsymbol{F}_{\rm R}\boldsymbol{f}_{{\rm B},k}[n],\ \forall k,n, \tag{20c}$$

$$\boldsymbol{y}_{m,k}[n] = \boldsymbol{\Xi}_m\boldsymbol{x}_k[n],\ \forall m,k,n, \tag{20d}$$

$$\boldsymbol{F}_{\rm R} = {\rm blkdiag}\left\{\boldsymbol{F}_{{\rm R},1},\ldots,\boldsymbol{F}_{{\rm R},M}\right\}, \tag{20e}$$

$$\left|[\boldsymbol{F}_{{\rm R},m}]_{i,j}\right| = 1,\ \forall i,j,m, \tag{20f}$$

where $\mathcal{Z} \triangleq \{\boldsymbol{F}_{\rm R}, \{\boldsymbol{f}_{{\rm B},k}[n], \boldsymbol{x}_k[n], \boldsymbol{y}_{m,k}[n], w_k[n], a_k[n]\}\}$ and the MSE can be equivalently written as

$$\bar{e}_k[n] \triangleq \left|1 - a_k^*[n]\bar{\boldsymbol{h}}_k^{\rm H}[n]\boldsymbol{x}_k[n]\right|^2 + \left|a_k[n]\right|^2\left(\sigma_{\rm z}^2 + \sum_{u\neq k}^{K}\left|\bar{\boldsymbol{h}}_k^{\rm H}[n]\boldsymbol{x}_u[n]\right|^2\right). \tag{21}$$

Furthermore, we consider using augmented Lagrangian (AL) methods to handle the equality constraints (20c) and (20d). Specifically, we introduce a penalty parameter ρ, and the multipliers $\boldsymbol{\Lambda}_{k,n}$'s and $\boldsymbol{\Gamma}_{m,k,n}$'s for (20c) and (20d), respectively. By constructing an AL function, we can move the equality constraints into the objective function. Thus, problem (20) can be equivalently transformed into an AL problem:

$$\begin{aligned}\min_{\mathcal{Z},\rho,\{\boldsymbol{\Lambda}_{k,n},\boldsymbol{\Gamma}_{m,k,n}\}} & \sum_{k=1}^{K}\sum_{n=1}^{N_{\rm c}}\left(w_k[n]\bar{e}_k[n] - \log\left(w_k[n]\right)\right) + \sum_{k=1}^{K}\sum_{n=1}^{N_{\rm c}}\frac{1}{2\rho}\left\|\boldsymbol{x}_k[n] - \boldsymbol{F}_{\rm R}\boldsymbol{f}_{{\rm B},k}[n] + \rho\boldsymbol{\Lambda}_{k,n}\right\|^2 \\ & + \sum_{m=1}^{M}\sum_{k=1}^{K}\sum_{n=1}^{N_{\rm c}}\frac{1}{2\rho}\left\|\boldsymbol{y}_{m,k}[n] - \boldsymbol{\Xi}_m\boldsymbol{x}_k[n] + \rho\boldsymbol{\Gamma}_{m,k,n}\right\|^2 \end{aligned} \tag{22a}$$

$$\text{s.t.} \qquad \text{(20b), (20e), and (20f).} \tag{22b}$$

Note that problem (22) can be solved efficiently by block coordinate descent (BCD) methods due to its separable variables. Thus, a double-loop algorithm can be applied by using the PDD framework [22].

For the inner loop, with the fixed penalty parameter ρ and multipliers $\boldsymbol{\Lambda}_{k,n}$'s and $\boldsymbol{\Gamma}_{m,k,n}$'s, we correspondingly deal with one block of the six block variables, i.e., $\{a_k[n]\}$, $\{w_k[n]\}$, $\boldsymbol{F}_{\rm R}$, $\{\boldsymbol{f}_{{\rm B},k}[n]\}$, $\{\boldsymbol{x}_k[n]\}$ and $\{\boldsymbol{y}_{m,k}[n]\}$, while fixing the other five blocks. This leads to the following six kinds of subproblems in each BCD iteration.

(1) The subproblem w.r.t. $a_k[n]$. The variable $a_k[n]$ is updated by solving the following subproblem:

$$\min_{a_k[n]} J_k[n]\left|a_k[n]\right|^2 - 2\Re\left\{a_k^*[n]\bar{\boldsymbol{h}}_k^{\rm H}[n]\boldsymbol{x}_k[n]\right\}, \tag{23}$$

where $J_k[n] = \sigma_z^2 + \sum_{u=1}^{K}\left|\bar{\boldsymbol{h}}_k^{\rm H}[n]\boldsymbol{x}_u[n]\right|^2$. The optimal solution is the well-known minimum MSE (MMSE) receiver given by

$$a_k[n] = J_k^{-1}[n]\bar{\boldsymbol{h}}_k^{\rm H}[n]\boldsymbol{x}_k[n]. \tag{24}$$

(2) The subproblem w.r.t. $w_k[n]$. Given the MMSE receiver in (24), the optimal weight can be expressed as

$$\begin{aligned} w_k[n] &= \arg\min_{w_k[n]} w_k[n]\bar{e}_k[n] - \log\left(w_k[n]\right) \\ &= \bar{e}_k^{-1}[n] \end{aligned}$$

$$= \left(1 - a_k^*[n]\bar{\boldsymbol{h}}_k^{\mathrm{H}}[n]\boldsymbol{x}_k[n]\right)^{-1}. \tag{25}$$

(3) The subproblem w.r.t. $\boldsymbol{F}_{\mathrm{R}}$. The subproblem with respect to variable $\boldsymbol{F}_{\mathrm{R}}$ is given by

$$\min_{|[\boldsymbol{F}_{\mathrm{R},m}]_{i,j}|=1} \sum_{k=1}^{K}\sum_{n=1}^{N_{\mathrm{c}}} \left\|\boldsymbol{x}_k[n] - \boldsymbol{F}_{\mathrm{R}}\boldsymbol{f}_{\mathrm{B},k}[n] + \rho\boldsymbol{\Lambda}_{k,n}\right\|^2. \tag{26}$$

In this subproblem, an optimal frequency-flat RF precoder should be achieved to balance the digital precoders across all the subcarriers. As a result of the block diagonal structure of $\boldsymbol{F}_{\mathrm{R}}$, subproblem (26) can be decomposed into M parallel subproblems, each of which is written as

$$\min_{|[\boldsymbol{F}_{\mathrm{R},m}]_{i,j}|=1} \mathrm{Tr}\left\{\boldsymbol{F}_{\mathrm{R},m}^{\mathrm{H}}\boldsymbol{F}_{\mathrm{R},m}\boldsymbol{B}_m\right\} - 2\Re\left\{\mathrm{Tr}\left\{\boldsymbol{F}_{\mathrm{R},m}^{\mathrm{H}}\boldsymbol{X}_m\right\}\right\}, \tag{27}$$

where for simplicity, $\boldsymbol{B}_m$ and $\boldsymbol{X}_m$ are defined by

$$\boldsymbol{B}_m = \boldsymbol{\Xi}_m\left(\sum_{k=1}^{K}\sum_{n=1}^{N_{\mathrm{c}}} \boldsymbol{f}_{\mathrm{B},k}[n]\boldsymbol{f}_{\mathrm{B},k}^{\mathrm{H}}[n]\right), \tag{28a}$$

$$\boldsymbol{X}_m = \boldsymbol{\Xi}_m\left(\sum_{k=1}^{K}\sum_{n=1}^{N_{\mathrm{c}}} \left(\boldsymbol{x}_k[n] + \rho\boldsymbol{\Lambda}_{k,n}\right)\boldsymbol{f}_{\mathrm{B},k}^{\mathrm{H}}[n]\right). \tag{28b}$$

Since the unit modulus constraints are still separable, we can resort to the BCD method to address each parallel subproblem efficiently. It means that in each iteration, only one entry of $\boldsymbol{F}_{\mathrm{R},m}$ is updated while others are fixed. Note that with B-bit PSs, only 2^B discrete phases can be adjusted for each entry of $\boldsymbol{F}_{\mathrm{R},m}$ [12]. The BCD-type algorithm for subproblem (27) is listed in Algorithm 1. Please refer to Appendix B of [22] for its detailed derivation.

Algorithm 1 BCD-type algorithm for subproblem (27)

Input: B, $\boldsymbol{R}_m = \boldsymbol{F}_{\mathrm{R},m}$, and $\boldsymbol{Q}_m = \boldsymbol{R}_m\boldsymbol{X}_m$.

1: **repeat**
2: **for** $(i,j) \in \{1,2,\ldots,N_{\mathrm{A}}\} \times \{1,2,\ldots,N_{\mathrm{RF}}\}$ **do**
3: $b = [\boldsymbol{R}_m]_{i,j}[\boldsymbol{B}_m]_{j,j} - [\boldsymbol{Q}_m]_{i,j} + [\boldsymbol{X}_m]_{i,j}$;
4: $x = \begin{cases} \exp\{\jmath\phi_b\}, & \text{if } B = \infty, \\ \exp\left\{\jmath\frac{2\pi}{2^B}i^\star\right\}, & \text{otherwise,} \end{cases}$ where $\phi_b \in [0, 2\pi)$ is the phase of b and $i^\star = \arg\ \max_{i' \in \{0,\ldots,2^{B-1}\}}\ |\phi_b - \frac{2\pi i'}{2^B}|$;
5: $[\boldsymbol{Q}_m]_{i,:} = [\boldsymbol{Q}_m]_{i,:} + (x - [\boldsymbol{R}_m]_{i,j})[\boldsymbol{B}_m]_{j,:}$;
6: $[\boldsymbol{R}_m]_{i,j} = x$;
7: **end for**
8: **until** some termination criterion is satisfied.

Output: $\boldsymbol{F}_{\mathrm{R},m} = \boldsymbol{R}_m$.

(4) The subproblem w.r.t. $\boldsymbol{f}_{\mathrm{B},k}[n]$. The variable $\boldsymbol{f}_{\mathrm{B},k}[n]$ is updated by solving the following unconstrained quadratic optimization subproblem:

$$\min_{\boldsymbol{f}_{\mathrm{B},k}[n]} \left\|\boldsymbol{x}_k[n] - \boldsymbol{F}_{\mathrm{R}}\boldsymbol{f}_{\mathrm{B},k}[n] + \rho\boldsymbol{\Lambda}_{k,n}\right\|^2. \tag{29}$$

Different from the previous subproblem with respect to $\boldsymbol{F}_{\mathrm{R}}$, each optimal frequency-selective digital precoder can be individually obtained as

$$\boldsymbol{f}_{\mathrm{B},k}[n] = \mathrm{blkdiag}\left\{\boldsymbol{F}_{\mathrm{R},1}^{\dagger}, \ldots, \boldsymbol{F}_{\mathrm{R},m}^{\dagger}\right\}\left(\boldsymbol{x}_k[n] + \rho\boldsymbol{\Lambda}_{k,n}\right). \tag{30}$$

(5) The subproblem w.r.t. $\boldsymbol{x}_k[n]$. As a matter of fact, this auxiliary variable $\boldsymbol{x}_k[n]$ represents a combination of the digital and RF precoders without any power constraint. Thus, we need to design $\boldsymbol{x}_k[n]$ by satisfying three objectives. That is maximizing the spectral efficiency, approximating the practical hybrid

structure and gradually complying with the per-RAU power constraints. Through some mathematical operations, the subproblem with respect to the variable $\boldsymbol{x}_k[n]$ can be simplified to

$$\begin{aligned}\min_{\boldsymbol{x}_k[n]}\ & \boldsymbol{x}_k^{\mathrm{H}}[n]\boldsymbol{A}[n]\boldsymbol{x}_k[n]-2w_k[n]\Re\left\{a_k^*[n]\boldsymbol{h}_k^{\mathrm{H}}[n]\boldsymbol{x}_k[n]\right\}\\ &+\frac{1}{2\rho}\|\boldsymbol{x}_k[n]-\boldsymbol{F}_{\mathrm{R}}\boldsymbol{f}_{\mathrm{B},k}[n]+\rho\boldsymbol{\Lambda}_{k,n}\|^2+\frac{1}{2\rho}\|\bar{\boldsymbol{y}}_k[n]-\boldsymbol{x}_k[n]\|^2,\end{aligned}\tag{31}$$

where for simplicity, $\boldsymbol{A}[n]$ and $\bar{\boldsymbol{y}}_k[n]$ are defined by

$$\boldsymbol{A}[n]=\sum_{j=1}^{K}w_j[n]|a_j[n]|^2\boldsymbol{h}_j[n]\boldsymbol{h}_j^{\mathrm{H}}[n],\tag{32a}$$

$$\bar{\boldsymbol{y}}_k[n]=\left[\left(\boldsymbol{y}_{1,k}[n]+\rho\boldsymbol{\Gamma}_{1,k,n}\right)^{\mathrm{T}},\ldots,\left(\boldsymbol{y}_{M,k}[n]+\rho\boldsymbol{\Gamma}_{M,k,n}\right)^{\mathrm{T}}\right]^{\mathrm{T}}.\tag{32b}$$

The optimal solution is given by

$$\boldsymbol{x}_k[n]=\left(\rho\boldsymbol{A}[n]+\boldsymbol{I}\right)^{-1}\left(\rho w_k[n]a_k[n]\boldsymbol{h}_k[n]+\frac{1}{2}\left(\bar{\boldsymbol{y}}_k[n]+\boldsymbol{F}_{\mathrm{R}}\boldsymbol{f}_{\mathrm{B},k}[n]-\rho\boldsymbol{\Lambda}_{k,n}\right)\right).\tag{33}$$

(6) The subproblem w.r.t. $\boldsymbol{y}_{m,k}[n]$. The auxiliary variable $\boldsymbol{y}_{m,k}[n]$ related to the per-RAU power constraints can be updated by addressing the following subproblem:

$$\min_{\boldsymbol{y}_{m,k}[n]}\quad\sum_{m=1}^{M}\sum_{k=1}^{K}\sum_{n=1}^{N_{\mathrm{c}}}\frac{1}{2\rho}\|\boldsymbol{y}_{m,k}[n]-\boldsymbol{\Xi}_m\boldsymbol{x}_k[n]+\rho\boldsymbol{\Gamma}_{m,k,n}\|^2\tag{34a}$$

$$\text{s.t.}\quad\text{(20b)}.\tag{34b}$$

This convex problem equals to the projection on a sphere centered at the origin, which has a closed-form solution as

$$\boldsymbol{y}_{m,k}[n]=\begin{cases}\boldsymbol{\Xi}_m\boldsymbol{x}_k[n]-\rho\boldsymbol{\Gamma}_{m,k,n}, & \text{if } \Psi_m\leqslant P_{\max}^{\mathrm{rau}},\\ \sqrt{\dfrac{P_{\max}^{\mathrm{rau}}}{\Psi_m}}\left(\boldsymbol{\Xi}_m\boldsymbol{x}_k[n]-\rho\boldsymbol{\Gamma}_{m,k,n}\right), & \text{otherwise},\end{cases}\tag{35}$$

where $\Psi_m\triangleq\sum_{k=1}^{K}\sum_{n=1}^{N_{\mathrm{c}}}\|\boldsymbol{\Xi}_m\boldsymbol{x}_k[n]-\rho\boldsymbol{\Gamma}_{m,k,n}\|^2$.

For the outer loop, we update the multipliers $\{\boldsymbol{\Lambda}_{k,n}\}$ and $\{\boldsymbol{\Gamma}_{m,k,n}\}$, and the penalty parameter ρ in terms of a constraint violation condition $\Omega^{(t)}\leqslant\eta\cdot\Omega^{(t-1)}$ in iteration t [26], where

$$\Omega^{(t)}\triangleq\max_{m,k}\left\{\sqrt{\sum_{n=1}^{N_{\mathrm{c}}}\left\|\boldsymbol{x}_k^{(t)}[n]-\boldsymbol{F}_{\mathrm{R}}^{(t)}\boldsymbol{f}_{\mathrm{B},k}^{(t)}[n]\right\|^2},\sqrt{\sum_{n=1}^{N_{\mathrm{c}}}\left\|\boldsymbol{y}_{m,k}^{(t)}[n]-\boldsymbol{\Xi}_m\boldsymbol{x}_k^{(t)}[n]\right\|^2}\right\}.\tag{36}$$

If this constraint violation condition is satisfied, the multipliers are updated as

$$\boldsymbol{\Lambda}_{k,n}^{(t+1)}=\boldsymbol{\Lambda}_{k,n}^{(t)}+\frac{1}{\rho^{(t)}}\left(\boldsymbol{x}_k^{(t)}[n]-\boldsymbol{F}_{\mathrm{R}}^{(t)}\boldsymbol{f}_{\mathrm{B},k}^{(t)}[n]\right),\tag{37a}$$

$$\boldsymbol{\Gamma}_{m,k,n}^{(t+1)}=\boldsymbol{\Gamma}_{m,k,n}^{(t)}+\frac{1}{\rho^{(t)}}\left(\boldsymbol{y}_{m,k}^{(t)}[n]-\boldsymbol{\Xi}_m\boldsymbol{x}_k^{(t)}[n]\right).\tag{37b}$$

Otherwise, the penalty parameter is updated according to

$$\rho^{(t+1)}=c\cdot\rho^{(t)},\tag{38}$$

where the predetermined constants $c\in(0,1)$ and $\eta\in(0,1)$ control the decline rate of ρ and measure the constraint violation, respectively.

Table 1 Simulation parameters

Parameter	Value
Zone radius R_0	120 m
Number of RAUs M	6
Number of antennas (RAU) N_{A}	8
Carrier frequency f_{c}	28 GHz
Subcarrier spacing $\triangle f$	60 kHz
Subcarrier number N_{c}	72
Guard interval N_{g}	16
Number of channel paths L	3
Path loss $\beta_{m,k}^2$	$\alpha + 10\beta \log_{10}(d) + \xi$ dB [a)]
Path delay distribution	$\mathcal{U}(\tau_0, \tau_0 + \Delta_\tau)$ [b)]
Path angle distribution	$\mathcal{U}(0, 2\pi)$

a) The values adopted for the model parameters are $\alpha = 72$, $\beta = 2.92$, and $\xi = 8.7$, respectively in [27]. d is the distance in meters.

b) τ_0 is the line-of-sight propagation time from one UE to one RAU and Δ_τ is the DS.

3.3 Complexity and convergence analysis

The proposed hybrid beamforming algorithm is summarized in Algorithm 2. Its main computational complexity lies in realizing the inner-loop optimization of problem (22) consisting of six subproblems. For each iteration, the complexity of solving (23), (25), (26), (29), (31) and (34) is $\mathcal{O}(KN_{\mathrm{c}}N_{\mathrm{A}}^{\mathrm{tot}})$, $\mathcal{O}(KN_{\mathrm{c}}N_{\mathrm{A}}^{\mathrm{tot}})$, $\mathcal{O}(I_1MN_{\mathrm{A}}^2N_{\mathrm{RF}}^2)$, $\mathcal{O}((N_{\mathrm{A}}^{\mathrm{tot}})^3 + KN_{\mathrm{c}}N_{\mathrm{A}}^{\mathrm{tot}}N_{\mathrm{RF}}^{\mathrm{tot}})$, $\mathcal{O}(N_{\mathrm{c}}(N_{\mathrm{A}}^{\mathrm{tot}})^3 + KN_{\mathrm{c}}(N_{\mathrm{A}}^{\mathrm{tot}})^2)$, and $\mathcal{O}(KN_{\mathrm{c}}N_{\mathrm{A}}^{\mathrm{tot}})$, respectively, where I_1 is the number of iterations consumed by Algorithm 1. In addition, for the convergence issue of Algorithm 2, one can check that the Robinson's condition holds for problem (20) at any limit point, which results in that the limit point of the sequence generated by this algorithm is a stationary point [23]. Furthermore, with the equivalence between problem (17) and problem (20), the proposed algorithm converges to the set of stationary solutions of problem (17). It is worth mentioning that for the case of finite-resolution PSs, the convergence result is not guaranteed due to its discrete phase values [22], while the simulation results still show good performance results by using the proposed algorithm.

Algorithm 2 Proposed hybrid beamforming algorithm

Input: $\boldsymbol{F}_R^{(0)}$, $\boldsymbol{f}_{\mathrm{B},k}^{(0)}[n]$, $\boldsymbol{x}_k^{(0)}[n]$, $\boldsymbol{y}_{m,k}^{(0)}[n]$, $\boldsymbol{\Lambda}_{k,n}^{(0)}$, and $\boldsymbol{\Gamma}_{m,k,n}^{(0)}$.
repeat
  repeat
    Update $a_{k,n}$ using Eq. (24);
    Update $w_{k,n}$ using Eq. (25);
    Update $\boldsymbol{F}_{\mathrm{R}}$ using Algorithm 1;
    Update $\boldsymbol{f}_{\mathrm{B},k}[n]$ using Eq. (30);
    Update $\boldsymbol{x}_k[n]$ using Eq. (33);
    Update $\boldsymbol{y}_{m,k}[n]$ using Eq. (35);
  until some termination criterion is satisfied;
  Update ρ, $\boldsymbol{\Lambda}_{k,n}$, and $\boldsymbol{\Gamma}_{m,k,n}$;
until some termination criterion is satisfied;
Output: $\boldsymbol{F}_{\mathrm{R}}$ and $\boldsymbol{f}_{\mathrm{B},k}[n]$.

4 Simulation results

In this section, the performance of hybrid beamforming for mmWave OFDM DASs with DSDs is evaluated in a simulation study. The simulation parameters are listed in Table 1. In Algorithm 2, we choose $\Omega^{(t)} \leqslant 10^{-3}$ as the termination condition, and set the control parameters to $c = 0.7$ and $\eta = 0.9$. The average rate is defined as

$$\bar{R}_k[n] = \frac{1}{KN_{\mathrm{c}}} \sum_{k=1}^{K} \sum_{n=1}^{N_{\mathrm{c}}} \log\left(1 + \frac{\left\|\boldsymbol{g}_k^{\mathrm{H}}[n]\boldsymbol{F}_{\mathrm{R}}\boldsymbol{f}_{\mathrm{B},k}[n]\right\|^2}{\sum_{u\neq k}^{K}\left\|\boldsymbol{g}_k^{\mathrm{H}}[n]\boldsymbol{F}_{\mathrm{R}}\boldsymbol{f}_{\mathrm{B},u}[n]\right\|^2 + \sigma_{\mathrm{z}}^2}\right). \tag{39}$$

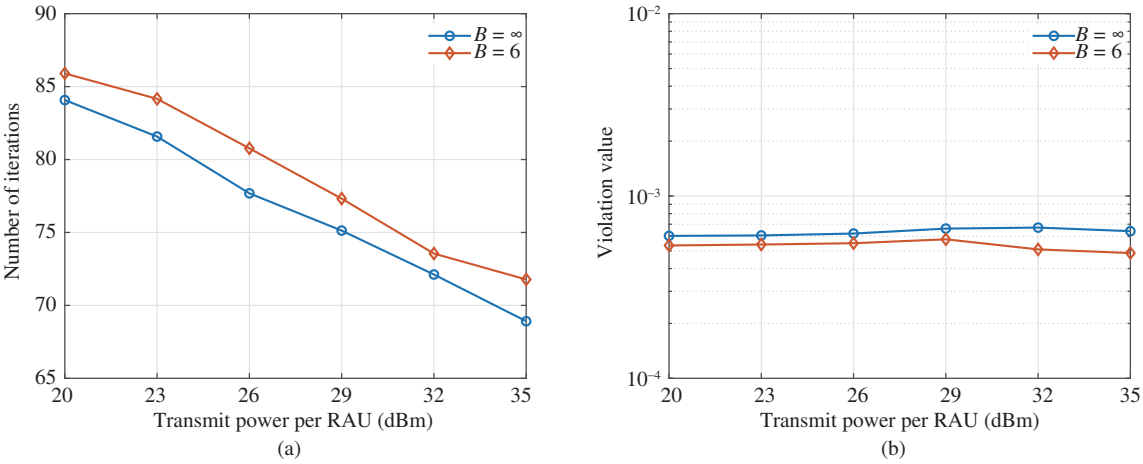

Figure 2 (Color online) Average convergence performance of Algorithm 2 versus per-RAU power with $K = 6$ and $N_{\mathrm{RF}} = 3$. (a) Number of iterations; (b) violation value.

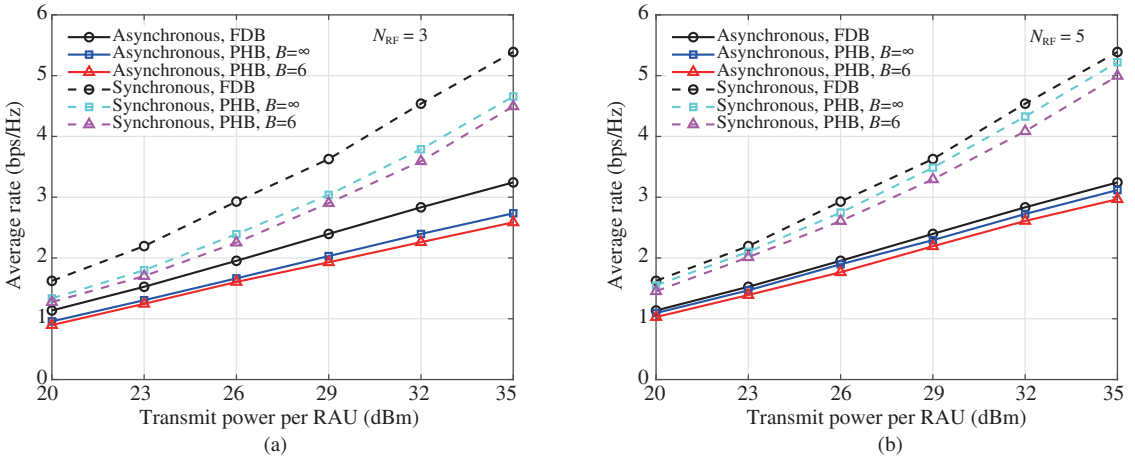

Figure 3 (Color online) Average rate versus per-RAU power with $K = 6$ and $P_{\max}^{\mathrm{rau}} = 30$ dBm for different number of RF chains. (a) $N_{\mathrm{RF}} = 3$; (b) $N_{\mathrm{RF}} = 5$.

Figure 2 shows the convergence performance of the proposed hybrid beamforming versus per-RAU transmitting power. Here, the number of iterations and violation values are plotted against the per-RAU transmitting power. Evidently, the average number of outer iterations ranges from 65 to 90 and decreases with increasing transmitting power per RAU, implying good convergence of the algorithm. Moreover, the average constraint violation is below the predetermined threshold 10^{-3}, indicating that the equality constraints (20c) and (20d) approximately hold. Consequently, the constraint of per-RAU transmitting power is well satisfied.

Synchronous reception for each UE is very challenging in DASs, because the transmitted signal from each RAU must simultaneously arrive at any UE. Hence, synchronous transmission (labeled 'Syn') can be served as a benchmark. In this scenario, perfect single-RAU synchronized channels and the differences in propagation times are available at the BPU, i.e., the equivalent DL channels in (13) are known. In the following, fully-digital beamforming is denoted as 'FDB'[1)], and our proposed hybrid beamforming algorithm is named as 'PHB'.

Figure 3 shows the average rates achieved by FDB and by PHB with infinite-resolution and 6-bit PSs, in both synchronous and asynchronous DL transmission cases. We first observe that the per-UE transmission rate of PHB improves when more RF chains are included at each RAU. When $N_{\mathrm{RF}} = 5$,

1) For comparison, we give a quasi-Newton method based FDB algorithm that works efficiently for OFDM DASs with per-RAU power constraints. This algorithm is derived in Appendix B.

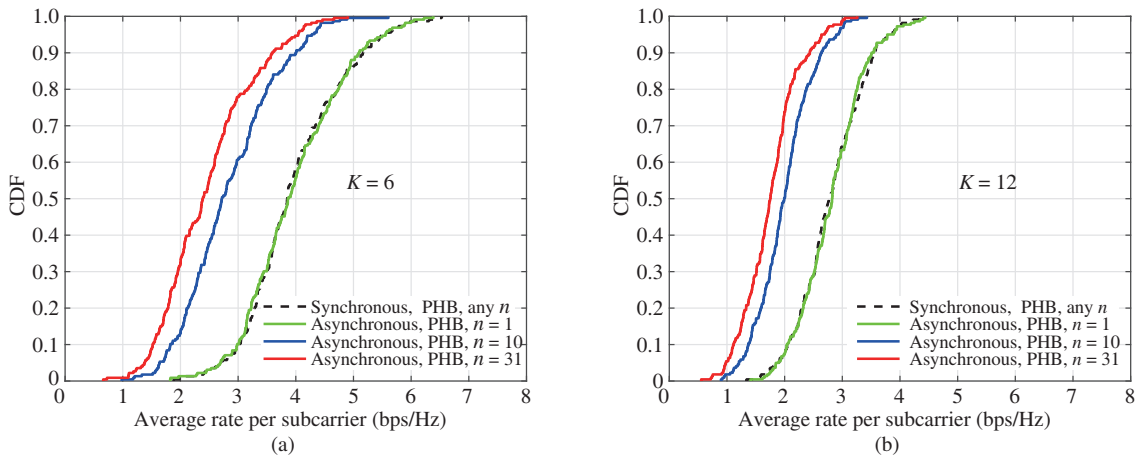

Figure 4 (Color online) CDF of average rate over different subcarriers with $M = 6$ and $P_{\max}^{\text{rau}} = 30$ dBm. (a) $K = 6$; (b) $K = 12$.

performance gain of PHB is comparable to that of FDB. Second, PHB with only 6-bit PSs achieves almost the same performance as the case of infinite-resolution PSs. Third, the DSDs significantly degrades the performance for both FDB and PHB, especially at high per-RAU transmitting power. In (13), the DSDs obviously increase the frequency selectivity of the original channels due to the synchronization error. As the BPU can access only the single-RAU synchronized DL channels of the UEs [20], the optimized hybrid precoders may not accurately align with the realistic mmWave channels when a phase error occurs.

Figure 4 shows the empirical cumulative distribution function (CDF) of the average rate over different subcarriers realized by PHB with 6-bit PSs. First, the average rate decreases with an increasing number of UEs because the transmitting power per RAU is finite. Furthermore, increasing the subcarrier index n increases the average rate gap between the synchronous and asynchronous cases. This trend manifests from the frequency-dependent phase shift in (13) induced by the DSDs. Last but not least, the average rate at the first subcarrier is identical in synchronous and asynchronous reception, because the subcarrier frequency of index 1 has zero phase shift of the propagation delay differences.

5 Conclusion

We have investigated hybrid beamforming in mmWave OFDM DASs. We first derived the equivalent DL channel model containing DSDs. We then designed a cooperative hybrid beamforming method based on the sum-utility maximization, which achieves comparable performance to fully-digital beamforming when used with both infinite-resolution and practical 6-bit PSs. In the simulations of the proposed hybrid beamforming algorithm, we confirmed that the DSDs significantly degraded the performance of the mmWave OFDM DASs.

Acknowledgements This work was supported in part by National Key Research and Development Program (Grant No. 2018YFE0205902), National Natural Science Foundation of China (NSFC) (Grant Nos. 61871122, 61971127), and Six Talent Peaks Project in Jiangsu Province.

Supporting information Appendixes A and B. The supporting information is available online at info.scichina.com and link.springer.com. The supporting materials are published as submitted, without typesetting or editing. The responsibility for scientific accuracy and content remains entirely with the authors.

References

1 Dai L. A comparative study on uplink sum capacity with co-located and distributed antennas. IEEE J Sel Areas Commun, 2011, 29: 1200–1213
2 Wang D M, Wang J Z, You X H, et al. Spectral efficiency of distributed MIMO systems. IEEE J Sel Areas Commun, 2013, 31: 2112–2127

3 Cao J, Wang D M, Li J M, et al. Uplink spectral efficiency analysis of multi-cell multi-user massive MIMO over correlated Ricean channel. Sci China Inf Sci, 2018, 61: 082305
4 Li L M, Wang D M, Niu X K, et al. mmWave communications for 5G: implementation challenges and advances. Sci China Inf Sci, 2018, 61: 021301
5 Bai L, Li T, Yu Q, et al. Cooperative multiuser beamforming in mmWave distributed antenna systems. IEEE Trans Veh Technol, 2018, 67: 12394–12397
6 Zhao L, Guo J J, Wei Z Q, et al. A distributed multi-RF chain hybrid mmWave scheme for small-cell systems. In: Proceedings of IEEE International Conference on Communications (ICC), Shanghai, 2019. 3393–3406
7 Yue D W, Xu S, Nguyen H H. Diversity gain of millimeter-wave massive MIMO systems with distributed antenna arrays. J Wirel Commun Netw, 2019, 2019: 54
8 Pi Z Y, Khan F. An introduction to millimeter-wave mobile broadband systems. IEEE Commun Mag, 2011, 49: 101–107
9 Talaei F, Dong X D. Hybrid mmWave MIMO-OFDM channel estimation based on the multi-band sparse structure of channel. IEEE Trans Commun, 2019, 67: 1018–1030
10 Kim J, Kim I G. Distributed antenna system-based millimeter-wave mobile broadband communication system for high speed trains. In: Proceedings of International Conference on ICT Convergence (ICTC), Jeju, 2013
11 Huo Y M, Dong X D, Lu T, et al. Distributed and multilayer UAV networks for next-generation wireless communication and power transfer: a feasibility study. IEEE Int Things J, 2019, 6: 7103–7115
12 Liang L, Xu W, Dong X D. Low-complexity hybrid precoding in massive multiuser MIMO systems. IEEE Wirel Commun Lett, 2014, 3: 653–656
13 Sohrabi F, Yu W. Hybrid analog and digital beamforming for mmWave OFDM large-scale antenna arrays. IEEE J Sel Areas Commun, 2017, 35: 1432–1443
14 Zhang J J, Huang Y M, Wang J H, et al. Hybrid precoding for wideband millimeter-wave systems with finite resolution phase shifters. IEEE Trans Veh Technol, 2018, 67: 11285–11290
15 Huo Y M, Dong X D, Xu W. 5G cellular user equipment: from theory to practical hardware design. IEEE Access, 2017, 5: 13992–14010
16 Huo Y M, Dong X D, Xu W, et al. Enabling multi-functional 5G and beyond user equipment: a survey and tutorial. IEEE Access, 2019, 7: 116975
17 Zhang Y, Huo Y M, Zhan J L, et al. ADMM enabled hybrid precoding in wideband distributed phased arrays based MIMO systems. In: Proceedings of IEEE Vehicular Technology Conference (VTC), Honolulu, 2019
18 Wang B L, Gao F F, Jin S, et al. Spatial- and frequency-wideband effects in millimeter-wave massive MIMO systems. IEEE Trans Signal Process, 2018, 66: 3393–3406
19 You L, Gao X Q, Li G Y, et al. BDMA for millimeter-wave/terahertz massive MIMO transmission with per-beam synchronization. IEEE J Sel Areas Commun, 2017, 35: 1550–1563
20 Yan H S, Lu I T. Asynchronous reception effects on distributed massive MIMO-OFDM system. IEEE Trans Commun, 2019, 67: 4782–4794
21 Feng Y, Wang M H, Wang D M, et al. Low complexity iterative detection for a large-scale distributed MIMO prototyping system. In: Proceedings of IEEE International Conference on Communications (ICC), Shanghai, 2019
22 Shi Q J, Hong M Y. Spectral efficiency optimization for millimeter wave multiuser MIMO systems. IEEE J Sel Top Signal Process, 2018, 12: 455–468
23 Shi Q J, Hong M Y. Penalty dual decomposition method with application in signal processing. In: Proceedings of IEEE International Conference on Acoustics, Speech and Signal Processing (ICASSP), New Orleans, 2017. 4059–4063
24 Huang J, Wang C X, Liu Y, et al. A novel 3D GBSM for mmWave MIMO channels. Sci China Inf Sci, 2018, 61: 102305
25 Shi Q J, Razaviyayn M, Luo Z Q, et al. An iteratively weighted MMSE approach to distributed sum-utility maximization for a MIMO interfering broadcast channel. IEEE Trans Signal Process, 2011, 59: 4331–4340
26 Bertsekas D P. Nonlinear Programming. 2nd ed. Belmont: Athena Scientific, 1999
27 Akdeniz M R, Liu Y P, Samimi M K, et al. Millimeter wave channel modeling and cellular capacity evaluation. IEEE J Sel Areas Commun, 2014, 32: 1164–1179